HAL
open science

High speed, antenna-enhanced 10.3 μm quantum cascade detector

G. Quinchard, C. Mismer, M. Hakl, J. Pereira, Quyang Lin, Sylvie Lepilliet, V. Trinité, A. Evirgen, Emilien Peytavit, J. Reverchon, et al.

▶ **To cite this version:**

G. Quinchard, C. Mismer, M. Hakl, J. Pereira, Quyang Lin, et al.. High speed, antenna-enhanced 10.3 μm quantum cascade detector. Applied Physics Letters, 2022, 120 (9), pp.091108. 10.1063/5.0078861 . hal-03598713

HAL Id: hal-03598713

https://hal.science/hal-03598713v1

Submitted on 7 Oct 2022

HAL is a multi-disciplinary open access archive for the deposit and dissemination of scientific research documents, whether they are published or not. The documents may come from teaching and research institutions in France or abroad, or from public or private research centers.

L'archive ouverte pluridisciplinaire **HAL**, est destinée au dépôt et à la diffusion de documents scientifiques de niveau recherche, publiés ou non, émanant des établissements d'enseignement et de recherche français ou étrangers, des laboratoires publics ou privés.

Applied Physics Letters

High speed, antenna-enhanced 10.3 μm quantum cascade detector

Cite as: Appl. Phys. Lett. **120**, 091108 (2022); https://doi.org/10.1063/5.0078861
Submitted: 13 December 2021 • Accepted: 11 February 2022 • Published Online: 01 March 2022

G. Quinchard, C. Mismer, M. Hakl, et al.

COLLECTIONS

This paper was selected as an Editor's Pick

View Online Export Citation CrossMark

ARTICLES YOU MAY BE INTERESTED IN

Silicon integrated terahertz quantum cascade ring laser frequency comb
Applied Physics Letters **120**, 091106 (2022); https://doi.org/10.1063/5.0078749

Electronic energy transport in nanoscale Au/Fe hetero-structures in the perspective of ultrafast lattice dynamics
Applied Physics Letters **120**, 092401 (2022); https://doi.org/10.1063/5.0080378

Long wavelength interband cascade lasers
Applied Physics Letters **120**, 091105 (2022); https://doi.org/10.1063/5.0084565

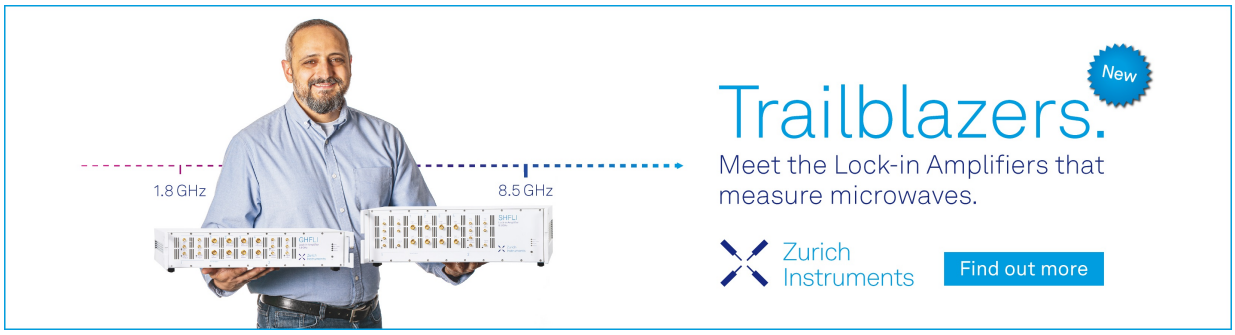

© 2022 Author(s).

Applied Physics Letters ARTICLE scitation.org/journal/apl

High speed, antenna-enhanced 10.3 μm quantum cascade detector

Cite as: Appl. Phys. Lett. **120**, 091108 (2022); doi: 10.1063/5.0078861
Submitted: 13 December 2021 · Accepted: 11 February 2022 ·
Published Online: 1 March 2022

View Online Export Citation CrossMark

G. Quinchard,[1] C. Mismer,[1] M. Hakl,[2] J. Pereira,[1] Q. Lin,[2] S. Lepillet,[2] V. Trinité,[1] A. Evirgen,[1] E. Peytavit,[2] J. L. Reverchon,[1,a)] J. F. Lampin,[2] S. Barbieri,[2] and A. Delga[1]

AFFILIATIONS

[1]III-VLab, a Joint Thales, Nokia and CEA-LETI Laboratory, Palaiseau, France
[2]IEMN, Institute of Electronics, Microelectronics and Nanotechnology, University of Lille, ISEN, CNRS, UMR 8520, 59652 Villeneuve d'Ascq, France

[a)]Author to whom correspondence should be addressed: jean-luc.reverchon@thalesgroup.com

ABSTRACT

The strong potential of intersubband detectors in the field of mid-infrared photodetection places this technology as a relevant alternative to HgCdTe detectors in the race for ultrafast operation. While their extremely short photocarrier's lifetime opens up possibilities of detection beyond 100 GHz, it is also the main reason for their comparatively high dark current. Here, a photovoltaic quantum cascade detector at 10.3 μm, embedded in a metal–metal patch antenna is presented in both direct and heterodyne detection schemes. In DC, a responsivity of 122 mA/W at 77 K and 85 mA/W at 295 K is reached. More strikingly, the device shows temperature independent heterodyne response with a capacitance-limited cutoff frequency of 25 GHz both at 77 K and room temperature. It is modeled quantitatively by means of an equivalent RC-circuit picture stemming from microscopic transport considerations.

Published under an exclusive license by AIP Publishing. https://doi.org/10.1063/5.0078861

Fast mid-infrared detectors are a key enabling technology for many applications such as dual comb spectroscopy,[1] secure free space optical (FSO) communications,[2,3] LIDAR,[4,5] or heterodyne interferometry for aperture synthesis.[6,7] For these applications, fast interband HgCdTe detectors are widely used since the first demonstration of a 1 GHz bandwidth, RC-limited heterodyne setup at 10.6 μm by Spears.[8] Important progress aimed at reducing the capacitance of devices allows us to reach an ultimate bandwidth of about 10 GHz,[9] mainly controlled by Shockley–Read–Hall (SRH) lifetimes in the ns range.

Intersubband (ISB) photodetectors, such as photoconductive quantum well infrared photodetectors (QWIPs)[10] and photovoltaic quantum cascade detectors (QCDs),[11] are well known for their extremely short carrier's relaxation time (~ps), leading to intrinsic frequency cutoffs in the 100 GHz range.[12–14] Pioneering demonstrations of ultrafast QWIPs[15] and QCDs[16–18] have reported frequency cutoffs beyond 20 GHz in mesa geometry, albeit with very small and/or thick devices to reduce the device parasitic capacitance. Thick detectors come at the price of a low sensitivity, because the internal gain scales as the inverse of the thickness while a small detector, typically 25 μm-diameter and below, is not practical for the most common system's implementation. Finally, fast non-radiative relaxation in ISB devices is the source of significant dark noise, which has limited their operation to cryogenic temperatures for direct detection schemes.

Recently, the demonstration of QWIPs coupled to patch antenna resonators (PARs) has drastically redefined the perspective of the ISB pathway.[19] Thanks to the antenna effect, this geometry allows one to obtain a photonic collection area much larger than the detector's electrical surface, i.e., the one generating dark current. In addition, it fulfills ISB polarization rules, allowing an efficient absorption under normal incidence, which leads to a significant increase in the signal-to-noise ratio.[20] Contrary to interband detectors, where passivation becomes a major issue because of a mid-gap SRH process for deep etched structures, ISB devices are unipolar and auto-passivated: the detection energy is deep below bandgap, making ISB detectors and PARs relevant altogether. Room temperature operation of both QWIPs[21] and QCDs[22] detectors embedded in metal–metal PARs has been reported in heterodyne detection schemes. A strong local oscillator (LO) is instrumental to overcome the dark current noise[23] and reach the LO photon-noise limited regime. It can be handled by ISB detectors thanks to their low saturation.[24]

Another asset of PARs is the reduction of the electrical area, which allows it to decrease the device capacitance, while maintaining the effective size of the detector. Combined with an efficient signal

Published under an exclusive license by AIP Publishing

extraction by means of a monolithically integrated coplanar waveguide (CPW), this has been used to demonstrate a QWIP with a flat response up to 70 GHz at room temperature.[25]

In this work, a $\lambda = 10.3\,\mu$m QCD embedded in a subwavelength PAR is presented. We first report the design and fabrication of an 8×8 QCD-PARs array co-integrated with a 50 Ω coplanar waveguide (CPW). Next, the device is characterized in DC with measured responsivities of 122 and 85 mA/W, respectively, at 77 and 295 K. Finally, an RC limited −3 dB cutoff frequency of 25 GHz at 295 K is obtained in the heterodyne configuration. The AC results, in particular, the weak thermal dependence of the responsivity, are explained through a microscopic approach that models the equivalent RC circuit of the PAR array. Thanks to the benefits of the PAR geometry and the co-integration with a CPW, these results compare favorably to all reported high speed QCD devices[16,18,22] in terms of gain and/or bandwidth.

The QCD coupled to the PAR array is described in Fig. 1. A five periods InGasAs/AlInAs QCD structure surrounded by Ohmic contacts made of 50 nm-thick n-doped InGaAs is grown by molecular beam epitaxy (MBE) on a 2-in. InP substrate. ISB absorption is tailored at 120 meV (10.3 μm) between states A_1 and B_5. The 306 nm thick active structure is embedded in a double metal (Au–Au) resonator through thermocompression wafer bonding on a metalized high resistivity Si substrate. The InP substrate is then selectively wet etched, and a 2D square matrix of 8×8 patches is finally obtained by inductively coupled Plasma (ICP) etching using an evaporated top metal mask. The band diagram of the structure under an applied bias of −0.4 V is shown in Fig. 1(e).

The parameters of the resulting $24 \times 24\ \mu m^2$ array are designed to optimize the collection of an incident laser beam at 10.3 μm. The size s of the patches is chosen to match the detection wavelength of the QCD according to the relation $s = \lambda/2n_{eff}$, with n_{eff} being the refractive index of the resonator. The array period p is then tuned to reach critical coupling between the incident light and the PAR array.[26] For the studied sample, the optimal parameters are found to be $s = 1.55\ \mu$m and $p = 3\ \mu$m. Finally, the patch antennas in the array are electrically connected by 20/80/200 nm thick Ti/Pt/Au wires obtained by electron-beam lithography and deposited on planarized SiO_2. As shown in Fig. 1(b), the wires are co-integrated with a 300 μm-long 50 Ω CPW to extract the signal by means of an RF probe.

The quality of the fabrication process of the QCD layer is first benchmarked with a series of DC measurements. Three checks are performed on dark current measurements (see Fig. 2). First, no surface currents are present. This was verified by comparing the dark currents of a 25 μm-side [shown in Fig. 2(a)] and a 50 μm-side square mesas (not shown). Within the measurement error, the two currents were identical. Second, the current is controlled by the QCD device. (i) The rectifying behavior, (ii) the negative differential resistance (NDR) regime predicted and visible at −0.6 V caused by long range resonant tunnelling[27,28] between levels A_1 and B_2, and generally (iii) the good agreement with our homemade model based on rate equations in the Wannier–Stark framework[29,30,37] are all evidence of a QCD limited transport. (A detailed comparison between the model and the experiment goes beyond the scope of this work.) Third, the activation energy E_a as a function of the applied bias, extracted from the thermal dependence of the dark current $J_{dark}(T) \propto \exp(-E_a/k_B T)$, shows a maximum of 89 meV at an applied bias of −0.4 V [Fig. 2(b)]. This value is

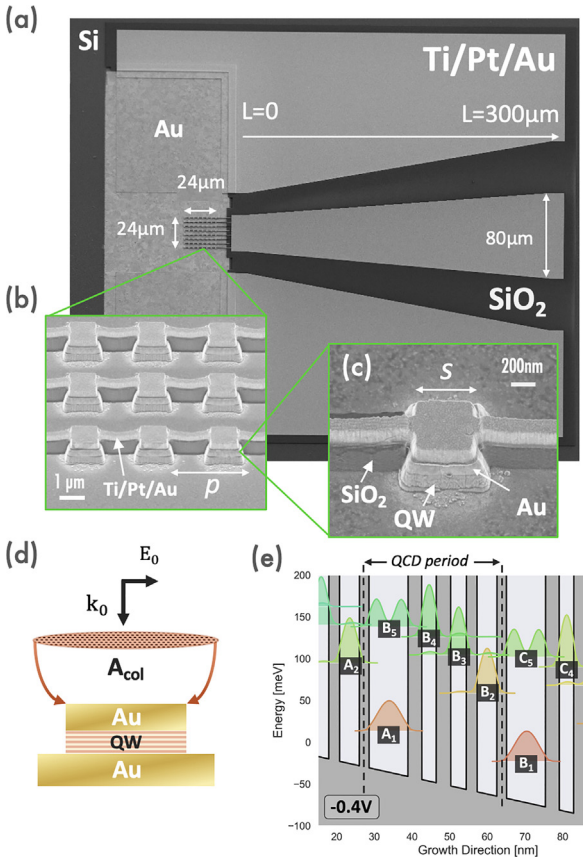

FIG. 1. (a) Scanning electron microscopy (SEM) picture of the 8×8 PAR array co-integrated with a 50 Ω CPW. (b) Close-up picture of the PAR-array with $p = 3\ \mu$m and $s = 1.55\ \mu$m. (c) Single patch antenna resonator containing the QCD active layer and connected with Ti/Pt/Au wires of 200 nm width. (d) Schematic of the PAR loaded by a QCD structure. Incident radiation of wave vector k_0 is collected over the effective area A_{col}. (e) Band structure and electronics states of the sample under an applied bias of −0.4 V (13 kV/cm). The stack for each period is **10.7**/3.6/**3.9**/3.8/**4.2**/2.8/**5.3**/2.5 nm, starting from the n-doped optically active quantum well ($n_{3D} = 6.7 \times 10^{17}$ cm^3). InGaAs layers are in bold, and AlInAs layers are in normal characters.

close to the theoretical maximum $E_{B_5} - E_{A_1}^{Fermi} = 95$ meV; at this bias parasitic diagonal transitions $A_1 - B_{1-4}$ are minimized.

Figure 3(a) shows the reflectivity (in red) and the normalized responsivity (in blue) spectra of the sample presented in Fig. 1 obtained by Fourier transform infrared spectroscopy (FTIR). The reflectivity spectrum was recorded under a 13 incidence angle with a DTGS (deuterated triglycine sulfate) MIR detector, while the responsivity spectrum was taken under normal incidence. Due to experimental constraints, the reflectivity and photocurrent spectra were recorded at different temperatures, however, the induced error is expected to be negligible. The reflectivity exhibits a minimum near the resonance wavelength of the cavity, tuned on the QCD optical transition. Although this design presents a high contrast at resonance (R = 12%), the critical coupling (R = 0%) is not fully achieved. Similarly to the reflectivity spectrum, the responsivity exhibits a double peak centered at 120 meV. This feature reveals a fortuitous strong coupling regime

Published under an exclusive license by AIP Publishing

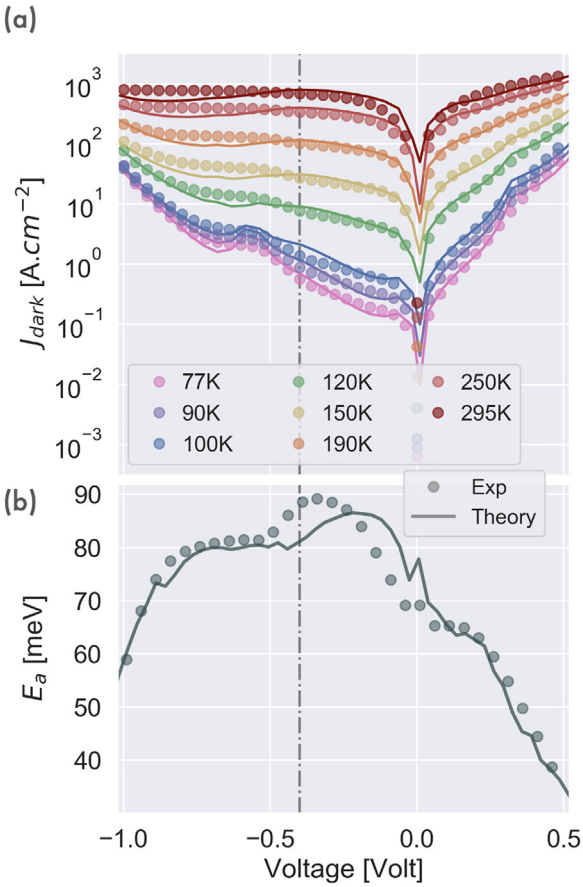

FIG. 2. (a) Experimental (dots) and theoretical (solid lines) dark current densities for a 25 × 25 μm^2 sample in mesa geometry. (b) Extracted activation energy E_a. Optimal bias (−0.4 V) is indicated by the dashed dotted line.

between the optical transition and the patch cavity mode, attributed to the high-doping of the active structure. Detailed investigations on the interplay between absorption and photoresponse, in particular, the key role played by intersubband polaritons can be found in a dedicated paper.[31]

The voltage dependence of the photocurrent under normal illumination by a 10.3 μm quantum cascade laser [QCL, green line in Fig. 3(a)] is plotted in Fig. 3(b) for several incident powers. The QCL was linearly polarized at 90 with respect to the wires connecting the patches, and we estimated a focused spot diameter of ∼25 μm through a knife-edge technique. The optical power was measured with a calibrated thermopile, taking into account the attenuation through the different optics and controlled attenuator. The photocurrent maximum is observed at −0.4 V, yielding responsivities of η = 122 mA/W at 77 K and η = 85 mA/W at 295 K for a QCL power of 0.6 mW. These correspond to external quantum efficiencies (EQE, photonic-to-electric conversion yield) EQE (77 K) = 1.47% and EQE (295 K) = 1.02%. The simultaneous optimization of the activation energy [see Fig. 2(b)] and responsivity at the same operating bias (−0.4 V, a small reverse bias to minimize dark noise[32]) illustrates the versatility of QCD design.

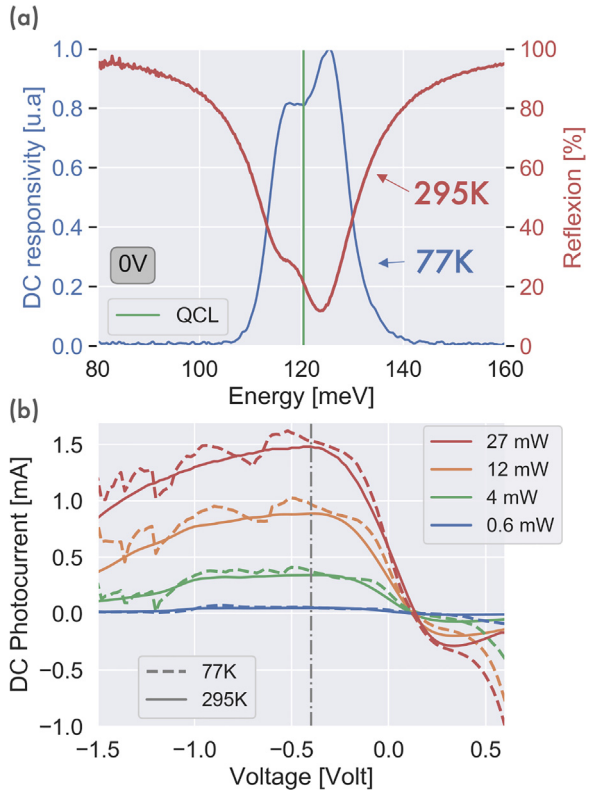

FIG. 3. (a) FTIR reflectivity and responsivity of the 8 × 8 PAR sample presented in Fig. 1. The emission line of a DFB quantum cascade laser emitting at 10.3 μm (120 meV) is shown by the green vertical line. (b) Voltage and power dependence of the photocurrent at 77 K (dashed lines) and room temperature (solid lines).

The small degradation of responsivity with temperature is striking. It can be roughly explained by a simple argument on the ISB rates Γ that control at first order the escape probability $p_e = \Gamma_{B_5\to B_4}/(\Gamma_{B_5\to B_4} + \Gamma_{B_5\to A_1})$. The tunnel rate $\Gamma_{B_5\to B_4}$ is constant with temperature, while the recombination rate $\Gamma_{B_5\to A_1}$ is mainly dominated by spontaneous emission of optical phonons even at room temperature. It represents a major difference with respect to QWIP detectors, where the probability of recapture of photo-carriers increases dramatically with temperature and results in a significant drop in responsivity.[33]

To complete the device DC characterization, we measured the evolution of the photocurrent with incident power. This is shown in Fig. S1 of the supplementary material. We find a saturation level of about 1 kW/cm^2 in agreement with published results[24] for comparable structures, illustrating the advantages of ISB detectors for heterodyne detection schemes. Indeed, these detectors are able to withstand strong local oscillator powers that can effectively act as signal amplifiers.[21]

The experimental setup used for the AC characterization is presented in Fig. S2 of the supplementary material. It is obtained by adding a second cw-distributed feedback (DFB) QCL, identical to the one used for the DC characterization, to provide the LO. The two lasers are temperature stabilized and driven by low noise current sources. The heterodyne beatnote resulting from the mixing of the two sources is collected by means of a cryogenic RF probe positioned at the edge of

Published under an exclusive license by AIP Publishing

the CPW and connected to a bias-T in order to extract the AC signal with the help of a spectrum analyzer (SA).

The heterodyne frequency response of the sample between 600 MHz and 67 GHz is presented in Fig. 4(a) at 77 and 295 K under an applied bias of −0.4 V. Each experimental point corresponds to the peak of the heterodyne beatnote recorded with the SA in a max-hold mode. The heterodyne power shown is not the direct measurement from the spectrum analyzer, but rather the *available* one obtained through a de-embedding process after removing the losses due to absorption in the RF cables and probes (see supplementary material S2 and S3). Indeed, at the PAR array-CPW interface [labeled L = 0 in Fig. 1(a)], there is a strong mismatch between the device impedance Z_{QCD} seen leftward in the plane L = 0 and the CPW and spectrum analyzer impedances (respectively, designed[34] and equal to 50 Ω). Therefore, a significant part of the generated heterodyne power is reflected at the L = 0 plane. Consequently, one has to distinguish between the *transmitted* power in a 50 Ω load, which corresponds to the measurement after loss corrections, and the *available* power that could be extracted through a matched load, i.e., for a load impedance Z_{load} equal to the QCD impedance Z_{QCD} seen leftward in the plane L = 0. These are linked by the relation

$$P_{available} = \frac{P_{transmitted}}{1 - |S_{11}|^2}, \tag{1}$$

with S_{11} being the device scattering parameter measured using a vector network analyzer (VNA). Since the *available* heterodyne power is the one most intrinsic to the device, it is the one presented here. Details of the de-embedding operation are presented in supplementary material S3.

The available heterodyne power shows a standard first order response with a −3 dB cutoff around 25 GHz. Consistently with results of DC measurements, we find also a very weak variation of P_{het} with temperature from 77 to 295 K. The expression of the heterodyne photocurrent at the frequency ω_h (the phase difference between the sources is neglected) is given by

$$I_{het}(\omega_h, t) = 2\eta\sqrt{P_{Sig}P_{LO}}\cos(\omega_h t). \tag{2}$$

The heterodyne power dissipated into the load, P_{het}, is given by

$$P_{het} = \frac{1}{2} Z_{load} |I_{load}|^2. \tag{3}$$

Here, P_{het} is by definition the power dissipated in the load: with the SA, $Z_{load} = 50\,\Omega$, and $P_{het} = P_{transmitted}$, while with a matched load $Z_{load} = Z^*_{QCD}$, therefore, $P_{het} = P_{available}$. In order to explain both the de-embedding process and the behavior of the heterodyne bandwidth, it is necessary to investigate and model of the PAR array impedance.

Z_{QCD} is extracted from the experimental S_{11} coefficients (plotted in Fig. S5 of the supplementary material) at 295 K. It is presented in Fig. 4(b) under the same illumination condition and bias used for the frequency response. In all measurements (bias, temperature, and illumination), the impedance of the device indicates an RC-like behavior with both decreasing positive resistance and negative reactance with increasing frequency. The 50 Ω characteristic impedance of the CPW and the load (SA or VNA) is plotted in red to highlight the strong impedance mismatch with the PAR array.

Following the impedance measurements, a RC model of the full QCD-PAR array is proposed to explain the observed temperature, power, and voltage dependence of the QCD-PAR array. It is shown in Fig. 4(c). Such RC macroscopic models are usually only inferred *ex post* from the fitting of the experimental data. In supplementary material S4, we show instead that our circuit model is obtained *ex ante* from an analysis at the microscopic level.

Macroscopically, the model shown in Fig. 4(c) describes the detector as a (i) current source I with an internal impedance $\mathscr{R}_{//}$ consisting of its (ii) dc photoresistance $\mathscr{R}_{opt}$ and (iii) dark current

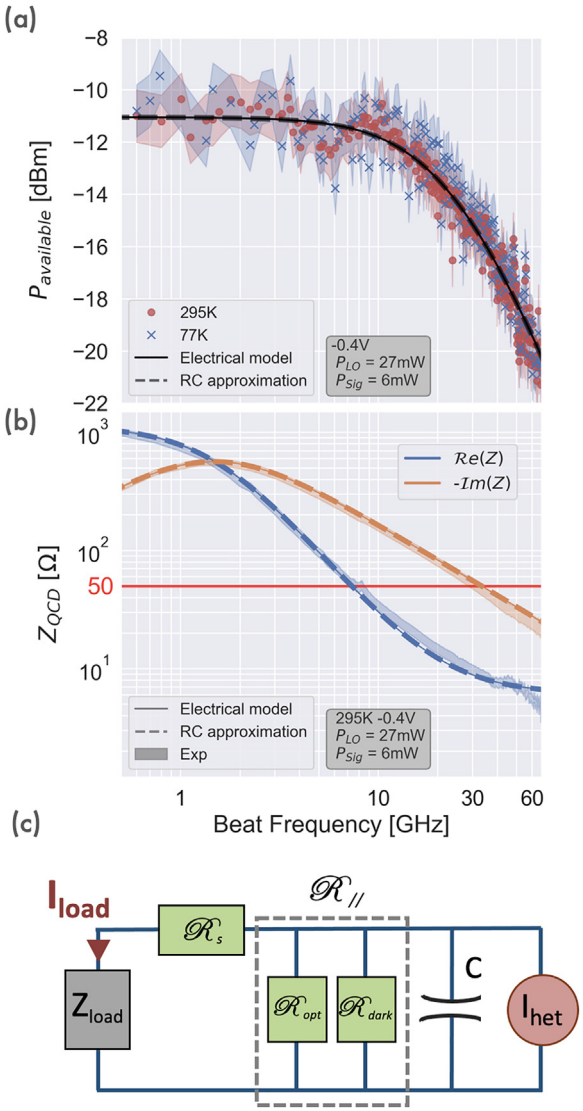

FIG. 4. *Available* heterodyne power (a) and impedance of the PAR array at 295 K (b) as seen in the $Z_{L=0}$ plane as a function of the frequency. The uncertainty (in shadow) on the power is due to the instability of the QCL sources due to optical feedback. The latter was minimized using an optical isolator. The uncertainty on the impedance comes from the error in determining the distance between the plane L = 0 and the RF probe used during the de-embedding process. (c) RC equivalent model of the PAR array.

Published under an exclusive license by AIP Publishing

TABLE I. Parameters of the RC equivalent circuit model extracted from experimental AC results compared with theoretical estimation and DC measurements (T = 295 K, bias = −0.4 V, P_{LO} = 27 mW, and P_{sig} = 6 mW).

	Experiment AC	Experiment DC	Theory
$\mathscr{R}_{//}$ (Ω)	1140.39	1193.73	1042.85
C (fF)	98.56	···	92.06
$\mathscr{R}_s$ (Ω)	5.07	···	5.58

resistance $\mathscr{R}_{dark}$, in parallel with the (iv) total capacitance C of the QCD-PAR array. Microscopically (at the level of a single period band structure), they, respectively, correspond to (i) the light-induced AC pumping of electrons in the upper B_5 and lower A_1 level of the ISB transition, to the (ii) light-induced and (iii) thermal DC pumping of electrons through the same ISB transition, and the (iv) plate capacitors created by the sheet charges in the ISB lower levels $A_1, B_1 \ldots$. The macroscopic series resistance $\mathscr{R}_s$ reflects only the resistance induced by the wires connecting the patches in the PAR array. No effect of intra-cascade transport [from states B_5 toward B_1 in Fig. 1(e)] was seen experimentally in the series resistance.

The extracted available heterodyne power and QCD impedance presented in Fig. 4 are reproduced quantitatively using both the full numerical calculation (solid line) and more importantly, an analytical RC approximation (dotted line, details in S4).

In Table I, the parameters fitted from the AC measurements using the RC model are in excellent agreement with values extracted from independent DC measurements and theoretical estimates. For $\mathscr{R}_{//}$, the DC experimental value is obtained from dark and photocurrent measurements using the differential resistance dV/dI, and the theoretical value is obtained using the model in supplementary material S4. The single patch capacitance $C = \varepsilon_{eff} s^2/e$ is estimated from effective dielectric function measurements,[35] and the series resistance is estimated from data available in the literature.[36] The fitted value of I_{het} gives a responsivity of 77 mA/W at 600 MHz, in good agreement with the value of the responsivity at 295 K obtained from the DC characterization. Supplementary material S6 shows that this agreement holds for a large panel of different experimental conditions when varying temperature, bias, and optical power.

The conclusion from the RF analysis is twofold: First, at the frequencies investigated (below 67 GHz), no internal transport mechanism limits the bandwidth, and the device is essentially capacitance limited. [Note that intra-cascade transport can be readily included as an additional series resistance to describe the ultimate intrinsic transit time cutoff, measured for QCDs around 160 GHz (Ref. 14).] Second, impedance matching is the crucial limiting parameter, in practice, for efficient signal extraction.

Compared to the responsivities found in this work, even at room temperature PAR-based QWIPs detectors demonstrated in Refs. 21 and 25 show values around 50%–100% higher: this stems from an extraction probability $p_e = 1$, whereas at 295 K, QCD will show $p_e \simeq 0.5 - 0.7$. However, this higher ultimate signal comes at the price of operation with higher currents leading to a higher noise. On the contrary, QCDs show lower noise and are more versatile in terms of operating conditions. This likely makes them easier to handle in terms of impedance matching using, e.g., commercially available trans-impedance amplifiers.

In this work, a room temperature 25 GHz 3 dB-bandwidth quantum cascade detector at 10.3 μm is demonstrated. We obtain responsivities of 122 and 85 mA/W at 77 and 295 K corresponding to external quantum efficiencies at 10.3 μm of 1.47% and 1.02%, respectively. Such high gain-bandwidth values are enabled by the patch antenna resonator architecture, as well as signal extraction through an integrated waveguide: the heterodyne beat from the mixing of two lasers is indeed recorded up to 67 GHz. A quantitative model based on microscopic and geometrical considerations allows us to understand and explain the RF behavior of the QCD structure as a function of the voltage, temperature, and incident power. It provides a simple RC picture of the device that could be exploited for the design of future QCDs.

See the supplementary material for further details about the experimental setup, the measurements, and the theoretical calculations.

This work was partially supported by the French National Research Agency, and Direction Générale de l'Armement (project HISPANID); Nord-Pas de Calais Regional Council; Fonds Européens de Développement Régional; RENATECH (French Network of Major Technology Centres); and CPER "Photonics for Society."

AUTHOR DECLARATIONS

Conflict of Interest

The authors declare no conflicts of interest.

DATA AVAILABILITY

The data that support the findings of this study are available from the corresponding author upon reasonable request.

REFERENCES

[1] I. Coddington, N. Newbury, and W. Swann, "Dual-comb spectroscopy," Optica **3**, 414–426 (2016).
[2] A. Delga and L. Leviandier, "Free-space optical communications with quantum cascade lasers," Proc. SPIE **10926**, 140–155 (2019).
[3] R. Martini, C. Glazowski, E. A. Whittaker, W. W. Harper, Y.-F. Su, J. F. Schultz, C. Gmachl, F. Capasso, D. L. Sivco, and A. Y. Cho, "Optical free-space communications at middle-infrared wavelengths," Proc. SPIE **5359**, 196–202 (2004).
[4] A. Samman, L. Rimai, J. McBride, R. Carter, W. Weber, C. Gmachl, F. Capasso, A. Hutchinson, D. Sivco, and A. Cho, "Potential use of near, mid and far infrared laser diodes in automotive LIDAR applications," in *Vehicular Technology Conference Fall 2000. IEEE VTS Fall VTC2000. 52nd Vehicular Technology Conference* (IEEE, 2000), Vol. 5, pp. 2084–2089.
[5] X. Yu and Y. Zhang, "Sense and avoid technologies with applications to unmanned aircraft systems: Review and prospects," Prog. Aerosp. Sci. **74**, 152–166 (2015).
[6] G. Bourdarot, H. Guillet de Chatellus, and J.-P. Berger, "Toward a large bandwidth photonic correlator for infrared heterodyne interferometry—A first laboratory proof of concept," Astron. Astrophys. **639**, A53 (2020).
[7] P. Krötz, D. Stupar, J. Krieg, G. Sonnabend, M. Sornig, F. Giorgetta, E. Baumann, M. Giovannini, N. Hoyler, D. Hofstetter, and R. Schieder, "Applications for quantum cascade lasers and detectors in mid-infrared high-resolution heterodyne astronomy," Appl. Phys. B **90**, 187–190 (2008).
[8] D. Spears, "Planar HgCdTe quadrantal heterodyne arrays with GHz response at 10.6 μm," Infrared Phys. **17**, 5–8 (1977).
[9] J. Rothman, "Physics and limitations of HgCdTe APDs: A review," J. Electron. Mater. **47**, 5657 (2018).

Published under an exclusive license by AIP Publishing

[10]B. Levine, C. Bethea, G. Hasnain, V. Shen, E. Pelve, R. Abbott, and S. Hsieh, "High sensitivity low dark current 10 μm GaAs quantum well infrared photodetectors," Appl. Phys. Lett. **56**, 851–853 (1990).
[11]L. Gendron, M. Carras, A. Huynh, V. Ortiz, C. Koeniguer, and V. Berger, "Quantum cascade photodetector," Appl. Phys. Lett. **85**, 2824–2826 (2004).
[12]B. K. Ridley, "Electron scattering by confined LO polar phonons in a quantum well," Phys. Rev. B **39**, 5282–5286 (1989).
[13]S. Ehret, H. Schneider, J. Fleissner, P. Koidl, and G. Böhm, "Ultrafast intersubband photocurrent response in quantum-well infrared photodetectors," Appl. Phys. Lett. **71**, 641–643 (1997).
[14]T. Dougakiuchi, A. Ito, M. Hitaka, K. Fujita, and M. Yamanishi, "Ultimate response time in mid-infrared high-speed low-noise quantum cascade detectors," Appl. Phys. Lett. **118**, 041101 (2021).
[15]P. Grant, R. Dudek, M. Buchanan, L. Wolfson, and H. Liu, "An ultra fast quantum well infrared photodetector," Infrared Phys. Technol. **47**, 144–152 (2005).
[16]D. Hofstetter, M. Graf, T. Aellen, J. Faist, L. Hvozdara, and S. Blaser, "23 GHz operation of a room temperature photovoltaic quantum cascade detector at 5.35 μm," Appl. Phys. Lett. **89**, 061119 (2006).
[17]Z. Xie, J. Huang, X. Chai, Z. Deng, Y. Chen, Q. Lu, Z. Xu, J. Chen, Y. Zhou, and B. Chen, "High-speed mid-wave infrared interband cascade photodetector at room temperature," Opt. Express **28**, 36915–36923 (2020).
[18]J. Hillbrand, L. M. Krüger, S. D. Cin, H. Knötig, J. Heidrich, A. M. Andrews, G. Strasser, U. Keller, and B. Schwarz, "High-speed quantum cascade detector characterized with a mid-infrared femtosecond oscillator," Opt. Express **29**, 5774–5781 (2021).
[19]W. A. Beck and M. S. Mirotznik, "Microstrip antenna coupling for quantum-well infrared photodetectors," Infrared Phys. Technol. **42**, 189–198 (2001).
[20]D. Palaferri, Y. Todorov, A. Mottaghizadeh, G. Frucci, G. Biasiol, and C. Sirtori, "Ultra-subwavelength resonators for high temperature high performance quantum detectors," New J. Phys. **18**, 113016 (2016).
[21]D. Palaferri, Y. Todorov, A. Bigioli, A. Mottaghizadeh, D. Gacemi, A. Calabrese, A. Vasanelli, L. Li, A. G. Davies, E. H. Linfield, F. Kapsalidis, M. Beck, J. Faist, and C. Sirtori, "Room-temperature nine-μm-wavelength photodetectors and GHz-frequency heterodyne receivers," Nature **556**, 85–88 (2018).
[22]A. Bigioli, G. Armaroli, A. Vasanelli, D. Gacemi, Y. Todorov, D. Palaferri, L. Li, A. G. Davies, E. Linfield, and C. Sirtori, "Long-wavelength infrared photovoltaic heterodyne receivers using patch-antenna quantum cascade detectors," Appl. Phys. Lett. **116**, 161101 (2020).
[23]E. R. Brown, K. A. McIntosh, K. B. Nichols, F. W. Smith, and M. J. Manfra, "CO_2-laser heterodyne detection with GaAs/AlGaAs MQW structures," in *Quantum Well Intersubband Transition Physics and Devices*, edited by H. C. Liu, B. F. Levine, and J. Y. Andersson (Springer, Dordrecht, The Netherlands, 1994), pp. 207–220.
[24]K. L. Vodopyanov, V. Chazapis, C. C. Phillips, B. Sung, and J. S. Harris, "Intersubband absorption saturation study of narrow III-V multiple quantum wells in the $\lambda = 2.8$–9 μm spectral range," Semicond. Sci. Technol. **12**, 708–714 (1997).
[25]M. Hakl, Q. Lin, S. Lepillet, M. Billet, J.-F. Lampin, S. Pirotta, R. Colombelli, W. Wan, J. C. Cao, H. Li, E. Peytavit, and S. Barbieri, "Ultrafast quantum-well photodetectors operating at 10 μm with a flat frequency response up to 70 GHz at room temperature," ACS Photonics **8**, 464–471 (2021).
[26]Y. Todorov, L. Tosetto, J. Teissier, A. M. Andrews, P. Klang, R. Colombelli, I. Sagnes, G. Strasser, and C. Sirtori, "Optical properties of metal-dielectric-metal microcavities in the THz frequency range," Opt. Express **18**, 13886–13907 (2010).
[27]A. Buffaz, M. Carras, L. Doyennette, A. Nedelcu, X. Marcadet, and V. Berger, "Quantum cascade detectors for very long wave infrared detection," Appl. Phys. Lett. **96**, 172101 (2010).
[28]H. Willenberg, G. H. Döhler, and J. Faist, "Intersubband gain in a Bloch oscillator and quantum cascade laser," Phys. Rev. B **67**, 085315 (2003).
[29]V. Trinité, E. Ouerghemmi, V. Guériaux, M. Carras, A. Nedelcu, E. Costard, and J. Nagle, "Modelling of electronic transport in quantum well infrared photodetectors," Infrared Phys. Technol. **54**, 204–208 (2011).
[30]A. Delga, "Quantum cascade detectors: A review," in *Mid-Infrared Optoelectronics*, Woodhead Publishing Series in Electronic and Optical Materials, edited by E. Tournié and L. Cerutti (Woodhead Publishing, 2020), pp. 337–377.
[31]M. Lagrée, M. Jeannin, G. Quinchard, O. Ouznali, A. Evirgen, V. Trinité, R. Colombelli, and A. Delga, "Direct polariton-to-electron tunneling in quantum cascade detectors operating in the strong light-matter coupling regime," arXiv:2110.08060 (2021).
[32]A. Delga, L. Doyennette, M. Carras, V. Trinité, and P. Bois, "Johnson and shot noises in intersubband detectors," Appl. Phys. Lett. **102**, 163507 (2013).
[33]H. C. Liu and H. Schneider, *Quantum Well Infrared Photodetectors* (Springer, Berlin/Heidelberg, 2007).
[34]S. Bedair and I. Wolff, "Fast, accurate and simple approximate analytic formulas for calculating the parameters of supported coplanar waveguides for (M)MIC's," IEEE Trans. Microwave Theory Tech. **40**, 41–48 (1992).
[35]G. Quinchard, "Détecteur infrarouge hétérodyne á cascade quantique," Ph.D. thesis (Université de Lille, 2021).
[36]S. Karim, K. Maaz, G. Ali, and W. Ensinger, "Diameter dependent failure current density of gold nanowires," J. Phys. D **42**, 185403 (2009).
[37]R. Terazzi, "Transport in qunatum cascade lasers," Ph.D. thesis (ETH, 2015).

Published under an exclusive license by AIP Publishing